PHOTONICS Research

Single-mode sapphire fiber Bragg grating high-temperature sensor

Jiafeng Wu,[1,2] Xizhen Xu,[1,2,3] Jia He,[1,2] Zhuoda Li,[1,2] Zhiyong Bai,[1,2] Xiaoyu Weng,[1] Liwei Liu,[1] Junle Qu,[1] Yiping Wang,[1,2] and Jun He[1,2,4]

[1]State Key Laboratory of Radio Frequency Heterogeneous Integration, Key Laboratory of Optoelectronic Devices and Systems of Ministry of Education/Guangdong Province, College of Physics and Optoelectronic Engineering, Shenzhen University, Shenzhen 518060, China
[2]Shenzhen Key Laboratory of Photonic Devices and Sensing Systems for Internet of Things, Guangdong and Hong Kong Joint Research Centre for Optical Fibre Sensors, Shenzhen University, Shenzhen 518060, China
[3]e-mail: xizhenxu@szu.edu.cn
[4]e-mail: hejun07@szu.edu.cn

Received 12 June 2025; revised 2 September 2025; accepted 4 September 2025; posted 5 September 2025 (Doc. ID 570273); published 26 November 2025

Sapphire fiber has been widely utilized in ultra-high-temperature environments. A sapphire fiber Bragg grating (SFBG) is a potential high-temperature sensor, but the multimodal behavior results in a broadband reflection spectrum and poor precision. In this article, we report a helical tapered depressed cladding waveguide (HTDCW) by using a femtosecond laser direct writing technique to realize single-mode operation of SFBG. The HTDCW was created using helical negative refractive index modification by forming a depressed cladding. The helical pitch was set as 0.7 μm, and the helical diameter linearly increased from 10 μm to 60 μm along the tapered length of 10 mm. We fabricated this structure into a coreless silica fiber and inserted it between a single-mode fiber (SMF) and an SFBG. According to the simulation result and mode field measurement, such a structure can effectively suppress the higher-order modes of sapphire fiber, and the fundamental mode distribution can be obtained eventually. In addition, the HTDCW can reduce the mode field mismatch between sapphire fiber and SMF. Based on this method, we successfully obtained a single-mode reflection spectrum with a signal-to-noise ratio of 11 dB and a narrow −3 dB bandwidth of 0.62 nm. In addition, such a single-mode operation SFBG sensor can be employed to measure temperatures ranging from 25°C to 1600°C, exhibiting much better repeatability and stability.

https://doi.org/10.1364/PRJ.570273

1. INTRODUCTION

High-temperature measurement plays a critical role in various application fields, including energy, aviation, and gas-fired boilers. In the field of nuclear energy, the operating temperatures of next-generation reactors have progressively increased—from 300°C in pressurized water reactors to 1000°C in high-temperature gas-cooled reactors, and even up to 1500°C in very high-temperature gas-cooled reactors [1–3]. Accurate temperature measurement can prevent core overheating, thereby avoiding economic losses and safety hazards. For instance, the required accuracy is 3°C for high-temperature gas-cooled reactors and 1.2% at 1300°C for advanced test reactors [4,5]. Furthermore, in the field of aviation, the turbine inlet temperature often reaches 1700°C [6]. Accurate temperature measurement of turbine blades prevents overheating-induced stress rupture, for example, requiring a temperature accuracy of ±6°C at 1400°C [7]. Sapphire fiber possesses a melting point exceeding 2000°C and demonstrates favorable radiation resistance characteristics [8,9]. Besides, a sapphire fiber Bragg grating (SFBG) inscribed using a femtosecond laser is widely exploited to measure temperature and strain [10,11]. These sensors have been demonstrated to withstand 1900°C [12] and maintain stable operation at 1500°C for 1000 h [13]. Hence, SFBG sensors have significant application value in ultra-high-temperature environments.

However, sapphire fiber is a single-crystal fiber without the core-clad structure due to the limitation in fabrication techniques. Therefore, sapphire fiber is intrinsically multimodal. The modal excitation and energy distribution among the modes are easily affected by environmental perturbations in multimode fiber, which severely affects the measurement precision of SFBG-based sensors. Solving these problems fundamentally requires stabilizing or suppressing the higher-order modes (HOMs) in sapphire fiber. Several research studies have been reported, including added multimode fibers [14,15], fiber bending technique [16], tapered fiber structures [17,18], and the fabrication of single-mode waveguides [19–21], for

example, adding dozens of meters of multimode lead-in fibers to achieve mode-stabilized excitation, thereby generating relatively stable reflection spectra [15]. Meanwhile, some algorithms, such as long-wavelength edge detection [22] and the cross-correlation algorithm [13], can be used to increase the demodulation accuracy further. However, the peak searching dispersion remains at ±10 pm, which is still worse than the FBG inscribed in single-mode fiber (SMF) [23,24]. Fiber bending can enhance the loss of HOMs to achieve mode suppression. However, as the bending radius decreases, it would also induce significant fundamental mode loss, resulting in the difficulty of fundamental mode peak detection [16]. Fiber tapering serves as an effective mode suppressing technique. In 2006, Grobnic *et al.* demonstrated using a tapered SMF to suppress the HOMs in sapphire fiber, which was fabricated by a hydrogen-oxygen flame heating system [17]. Bian *et al.* employed electric discharge heating to taper and fusion splice the SMF and sapphire fiber, thereby forming an overlapped double-conical (ODC) structure [18]. However, the reflection spectra achieved by using these methods still exhibit split peaks rather than a single peak, which also hinders the accuracy and stability of peak detection. Moreover, tapered fiber structures fabricated via thermal processing methods exhibit limited precision in tapered region morphological control. Hence, the HOMs in sapphire fiber cannot be completely suppressed.

Femtosecond laser direct writing of single-mode waveguides in sapphire fibers provides a fundamental solution to the issues of multimode operation. Fabricating a single-mode depressed cladding waveguide and Bragg grating in sapphire fiber by using femtosecond laser direct writing can generate the single-mode Bragg resonance [19–21]. The spectral bandwidth can reach up to 0.18 nm, exhibiting an enhancement in the stability of temperature response [21]. However, due to the relatively high transmission loss (i.e., 1.5 dB/cm [20]) of the waveguide and its lower fabrication efficiency, there remains a challenge in fabricating a waveguide with a length exceeding 4 cm. Meanwhile, in high-temperature measurements, the length of the high-temperature zones extends beyond several centimeters, typically reaching approximately 10 cm in regions exceeding 1200°C [5,25–27]. An excessively short waveguide will cause the silica lead-in fiber to melt, resulting in sensor failure. Such a short single-mode SFBG can only withstand 1200°C, which is much lower than the operation temperature of typical SFBGs (1500°C or even 1900°C). Therefore, the development of a more practical single-mode operation SFBG sensor that can work at higher temperatures is essential.

In this article, we proposed and demonstrated a helical tapered depressed cladding waveguide (HTDCW) in coreless silica fiber by using the femtosecond laser direct writing technique. This approach will not damage the original structure of the fiber, thus maintaining its mechanical strength. We simulated and fabricated the HTDCW according to the adiabatic criterion. According to the mode field measurement, HOMs can be effectively suppressed, and the output mode field of HTDCW also exhibits an expanded fundamental mode field. Then, the spectra of SFBG were studied, and the results show that a single-mode reflection spectrum with a −3 dB bandwidth of 0.62 nm and a signal-to-noise ratio (SNR) of 11 dB can be obtained. Furthermore, such a single-mode SFBG sensor was furnace-tested up to 1600°C, which exhibited good repeatability and stability in temperature measurements. This sensor effectively addresses the challenges of poor temperature measurement stability and limited operational temperature range.

2. DEVICE DESIGN AND FABRICATION

As shown in Fig. 1, the sensor is composed of SMF, HTDCW, and SFBG. Note that we used the transversal helical scanning method to fabricate HTDCW instead of the linear translational scanning method. According to our previous works [21,28], the transversal helical scanning method has been demonstrated to create a waveguide with better guiding confinement, resulting in lower transmission loss. Meanwhile, as we all know, the conventional linear translational scanning method typically requires a segmented fabrication approach to maintain optical confinement across varying radii in a tapered waveguide [29,30]. It will introduce abrupt transitions at splicing points, leading to non-continuous waveguide profiles.

The schematic diagram of the experimental setup for the fabrication of an HTDCW and an SFBG is shown in Fig. 1. A femtosecond laser with a central wavelength of 515 nm, a pulse width of 245 fs, a repetition rate of 1 MHz, and a laser spot diameter of 3 mm was employed as the laser source. The output beam was expanded using a telescope, and the pulse energy was adjusted using a half-waveplate and a polarizer. A 100× Leica oil-immersion objective with a numerical aperture (N.A.) of 1.25 served as the focusing element. Note that the index-matching oil was applied to eliminate the distortion to the focus of the laser induced by the cylindrical geometry of the fiber. For the fabrication of HTDCW, a multimode coreless silica fiber (Thorlabs, FG125LA) with a diameter of 125 μm and a refractive index of 1.458 at 1550 nm was used. Meanwhile, a single-crystal sapphire fiber (Jingying Inc.) with a diameter of 60 μm and a refractive index of 1.745 at 1550 nm was employed for fabricating SFBG. Then, the fibers were moved precisely using a three-dimensional air-bearing translation stage (Aus-precision, QFL-100XY for x and y axes, and RBN-Z-5 for the z axis).

Shown in Fig. 1(a) is the working principle of the HTDCW. On one hand, when the incident light is launched from the SMF into the HTDCW, the critical angle θ_{crit} gradually decreases. The fundamental mode maintains stable propagation without coupling to HOMs. In this way, the output mode field distribution at port 2 of the HTDCW can maintain the expanded fundamental mode field. In addition, owing to the decreased mode field mismatch with sapphire fiber, the excitation efficiency of HOMs in sapphire fiber decreases [31]. Conversely, when the light is reflected from SFBG, the critical angle θ_{crit} progressively increases within HTDCW. As the light fails to fulfill the condition for total internal reflection, HOMs will couple into the cladding and attenuate. Eventually, at port 1 of the HTDCW, most of the HOMs will be suppressed, obtaining a fundamental mode field.

A schematic diagram of the cross-section of HTDCW is displayed in Fig. 1(b). The structure consists of three regions.

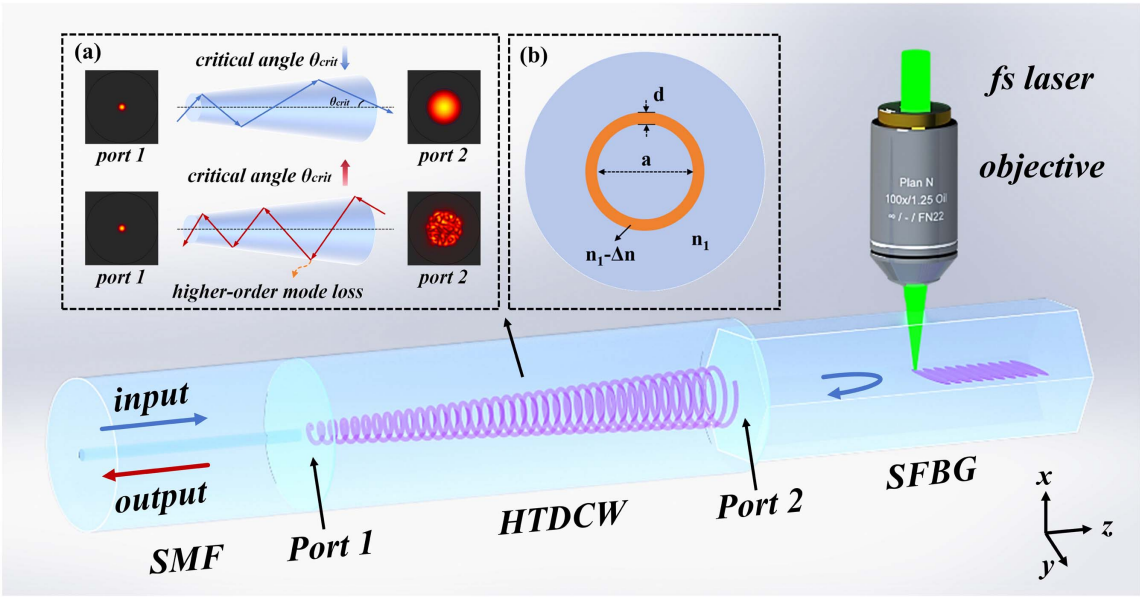

Fig. 1. Schematic of an HTDCW and an SFBG fabricated by femtosecond laser direct writing technique. (a) Simulated mode field and schematic diagram of the optical path during the light forward and reverse propagation through the HTDCW. (b) Schematic of the cross-section of HTDCW.

First is the core region, characterized by a refractive index of n_1 and a diameter of a. Next, the cladding region features a refractive index of $n_1 - \Delta n$, where Δn denotes the refractive index modification (RIM) induced by the femtosecond laser. This cladding region has a thickness of d. Finally, there is the outer-cladding region, whose refractive index equals that of the core, n_1. To optimize the waveguide structure and minimize the waveguide transmission loss, the loss of the fundamental mode under different values of RIM, cladding thickness, and core diameter was simulated, as shown in Fig. 2(a). The core diameter of HTDCW increases from D_1 (10 μm) to D_2 (60 μm), which corresponds to the SMF core diameter and the sapphire fiber diameter, respectively. When the core diameter is smaller, the fundamental mode loss becomes more sensitive to the changes of cladding thickness and RIM. Additionally, the fundamental mode loss of the waveguide with a core diameter of 10 μm is greater. It indicates that the transmission loss of HTDCW is predominantly concentrated in the smaller diameter section. Moreover, greater cladding thickness and RIM are beneficial for reducing the loss. However, to ensure the single-mode operation of the waveguide, we employed a cladding thickness d of 2 μm and an RIM Δn of 0.015, according to the previous work [28]. And the waveguide diameter linearly increases from 10 μm to 60 μm for inscribing the HTDCW in multimode coreless silica fiber.

For the tapered waveguide, an excessive taper angle will lead to higher transmission loss. To achieve the lower-loss transmission of the fundamental mode, the adiabatic criterion needs to be fulfilled [32]:

$$\Omega(z) \le \frac{a(z)(\beta_{01}(z) - \beta_{02}(z))}{2\pi}, \tag{1}$$

where z is the coordinate along the fiber axis, Ω is the taper angle, a is the core diameter, and β_{01} and β_{02} are the propagation constants of LP_{01} and LP_{02} modes, respectively. The propagation constant β is related to the effective refractive index n_{eff} by $\beta = 2\pi n_{\text{eff}}/\lambda$. As shown in Fig. 2(b), the n_{eff} of LP_{01} to LP_{04} modes in HTDCW at various core diameters were calculated by using finite element modeling. The inset of Fig. 2(b) plots the intensity profile of these four modes

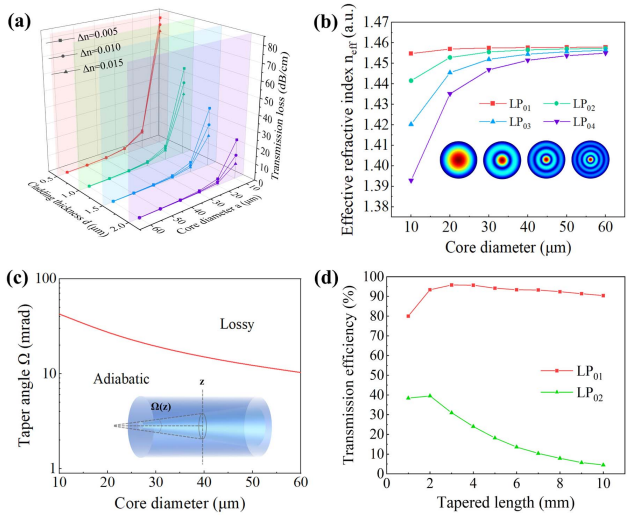

Fig. 2. (a) Theoretical calculation of the fundamental mode transmission loss in various cladding thicknesses, RIM values, and core diameters. (b) Calculated effective refractive index n_{eff} of LP_{01} to LP_{04} modes in HTDCW with a cladding thickness of 2 μm and an RIM of 0.015 versus different core diameters. (c) The calculated local taper angle for a core diameter varying from 10 μm to 60 μm according to the adiabatic criterion. (d) The transmission efficiency of LP_{01} and LP_{02} modes versus the different tapered lengths of HTDCW.

at the core diameter of 60 μm. Note that the waveguide structure of HTDCW used for the calculation is based on the parameters mentioned above. As can be observed, the n_{eff} of modes decrease and become more separate from each other as the core diameter decreases. According to Eq. (1), we calculated the taper angles that satisfy the adiabatic criterion in different core diameters, as illustrated in Fig. 2(c). The taper angles within the region below the red solid line comply with the adiabatic criterion. Theoretically, in such conditions, the fundamental mode can propagate with negligible loss. Then, we investigated the impact of taper angle on the suppression efficiency of HOMs. The core diameter linearly decreases from D_2 to D_1, where D_1 is 10 μm and D_2 is 60 μm. Therefore, the taper angle Ω can be defined as

$$\Omega = 2\arctan\left(\frac{D_2 - D_1}{2L}\right), \tag{2}$$

where L is the tapered length of the HTDCW. According to the adiabatic criterion, the calculated taper angle should be less than 10.3 mrad. It implies that the tapered length must exceed 4.85 mm. As illustrated in Fig. 2(d), the transmission efficiency of the LP_{01} mode reaches its maximum value of 95% when the tapered length is 4 mm. However, the transmission efficiency of LP_{02} mode remains at 20%. To suppress the HOMs as thoroughly as possible, we extended the length of the tapered region to increase the number of light reflections within the HTDCW, which in turn enhanced the loss of HOMs. As a result, the transmission efficiency of the LP_{02} mode could be reduced to 4.5% at the tapered length of 10 mm, while the LP_{01} mode maintains a transmission efficiency of 90%. Therefore, a single-mode operation can be achieved by using these structural parameters.

Then, the HTDCW was fabricated using the transversal helical scanning method. At first, the coreless silica fiber with a length of 10 mm was fusion spliced with two segments of SMF (Corning, G652D). Then, the laser was focused into the coreless fiber using a pulse energy of 22 nJ and 0.3 mm/s writing speed at a repetition rate of 1 MHz. The spliced fibers were translated in a tapered helical trajectory via synchronous movements along the x, y, and z axes. Figure 3(a) presents the schematic diagram of the HTDCW. We characterized the morphology and refractive index distribution at three distinct locations of HTDCW. As shown in the insets of Figs. 3(b1)–3(b3), the helical pitch was set as 0.7 μm, while the laser modulation spot size was approximately 1 μm, creating an overlap. This design ensures the axial confinement during waveguide inscription. In addition, for coreless silica fiber, the helical pitch of 0.7 μm corresponds to the resonant Bragg wavelength of 1 μm (second-order FBG) and 2 μm (first-order FBG), thereby preventing spectral interference with the SFBG that has a resonant wavelength of approximately 1.55 μm. The helical waveguide diameter linearly increased from 10 μm to 60 μm along the tapered length of 10 mm. Finally, the HTDCW was inscribed into the coreless silica fiber. As shown in Figs. 3(b1)–3(b3), the HTDCW was precisely inscribed into the middle of the coreless silica fiber, and the core diameter continuously increases along the z axis. Moreover, as shown in Figs. 3(c1)–3(c3), the cross-section microscope images reveal that the HTDCW maintains a circular geometry. Hence, the waveguide

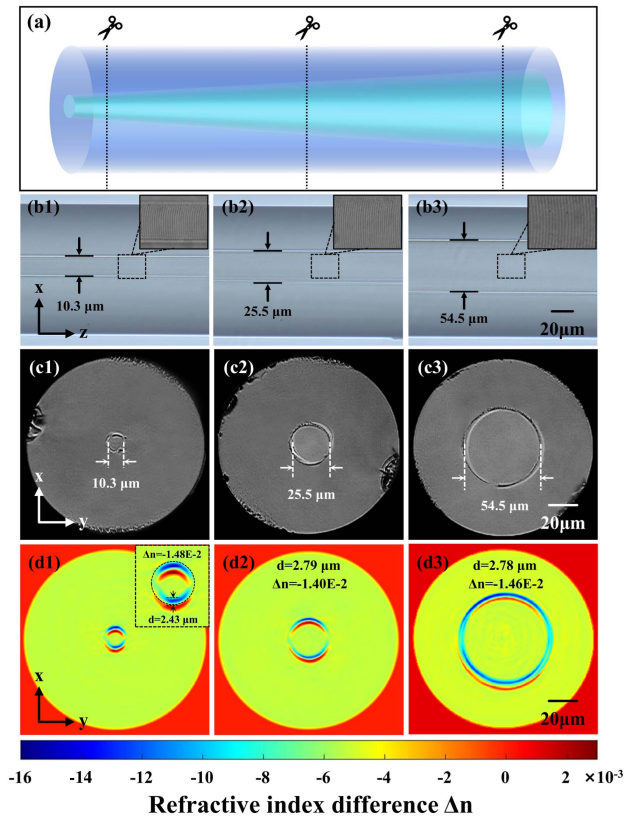

Fig. 3. (a) Schematic of HTDCW. (b) Microscope images of the top view of HTDCW in three regions. Inset: locally magnified images of the top view of HTDCW captured by a 100× oil immersion objective. (c) Microscope images of the cross-section view of HTDCW in three regions. (d) Refractive index modulation distribution of HTDCW in three regions.

can maintain well-guiding confinement characteristics using the transversal helical scanning method.

Subsequently, the RIM distribution was measured by using digital holographic microscopy (SHR-1602, Shanghai University) with an index accuracy of 10^{-4}. As illustrated in Figs. 3(d1)–3(d3), the cross-sectional RIM distribution of HTDCW at three regions is presented. It can be seen that the RIM distribution consists of positive and negative refractive index changes. This phenomenon can be attributed to the use of higher pulse energy, which induces type III modification in the fused silica under femtosecond laser irradiation [33,34]. When the pulse energy exceeds a critical threshold and the localized temperature reaches the glass softening point, a micro-explosion occurs due to high pressures in a confined volume of the material. This results in shock waves that are responsible for the localized modification of glass, forming a void or less dense material surrounded by densified material [35–37]. The waveguide core is formed by leaving the core unmodified, and the negative RIM area forms the waveguide cladding. The cladding thickness d of the waveguide at the three regions is 2.43 μm, 2.79 μm, and 2.78 μm. And the refractive index modification Δn is -1.48×10^{-2}, -1.40×10^{-2}, and -1.46×10^{-2}, respectively. Note that the fabricated HTDCW exhibits close agreement with the simulated

structural parameters. It can be attributed to the HTDCW being precisely inscribed by using the femtosecond laser direct writing technique.

3. DEVICE MEASUREMENT AND ANALYSIS

We further characterized the transmission mode near-field profile of the fabricated HTDCW and sapphire fiber by using the experimental setup illustrated in Fig. 4(a). A linearly polarized laser beam was generated from a tunable laser (Keysight, 81940A). And a mode observation system consisting of the objective lens and CCD (Newport, LBP2-HR-IR2) was set up to measure the near-field profiles. At first, we studied the ability of HTDCW on the fundamental mode field expansion. As illustrated in Fig. 4(b), we used an SMF as a lead-in fiber to butt-couple it to port 1 of the HTDCW. Light with a wavelength of 1553.8 nm from a tunable laser was incident on both the lead-in SMF and the HTDCW. Then, we measured the near-field profile of SMF and port 2 of the HTDCW. It can be found in Figs. 4(d), 4(e) that the SMF mode field diameter of 10 μm can expand to dimensions of 22.7 μm × 17.0 μm through HTDCW. And the mode field can substantially maintain a fundamental mode field distribution. It indicates that this mode field keeps a single-mode characteristic without generating HOMs. This is beneficial for improving the mode field matching between SMF and sapphire fiber, thereby reducing the coupling loss of the fundamental mode [31].

Then, we measured the capability of HTDCW to suppress the HOMs. As illustrated in Fig. 4(c), to excite as many HOMs as possible within the sapphire fiber with a length of 10 cm, a 62.5/125 μm multimode silica fiber (MMF, i.e., lead-in fiber) with a length of 1 m was butt-coupled to the sapphire fiber. And the joint was immersed in the index-matching oil. Then we measured the near-field profile of the sapphire fiber. As shown in Fig. 4(f), multimode operation could be seen from the transmission mode near-field profile of the sapphire fiber. Then, port 2 of HTDCW was butt-coupled to the end face of the sapphire fiber, and we measured the near-field profile of port 1 of HTDCW. Figure 4(g) exhibits a fundamental mode field distribution with dimensions of 11.0 μm × 8.5 μm, which is close to the mode field diameter of SMF. It indicates that the HOMs in sapphire fiber could be suppressed after the light passes through the HTDCW. And part of the HOMs were converted to the fundamental mode, significantly enhancing the SNR. The residual HOMs could be attenuated after entering the subsequent SMF segment. Hence, as illustrated in Figs. 1(b) and 3(d1)–3(d3), despite deviations between the designed and fabricated HTDCW (attributed to positive index modification), the device still achieved effective light guidance and good HOMs suppression as indicated by the near-field profile results.

Furthermore, as displayed in the inset of Fig. 5(a), we have investigated the spectral characteristics of the SFBG measured by butt-coupling to MMF (T1), SMF (T2), and the HTDCW (T3). The SFBG was fabricated by using a femtosecond laser line-by-line scanning technique [38]. The fabrication parameters, including pulse energy, scanning velocity, track length, and repetition rate, were set as 45 nJ, 0.3 mm/s, 40 μm, and 200 kHz. Then, the SFBG with a grating period of 1.78 μm and a grating length of 4 mm was inscribed into the tip of the sapphire fiber. The distance between the coupling point and the

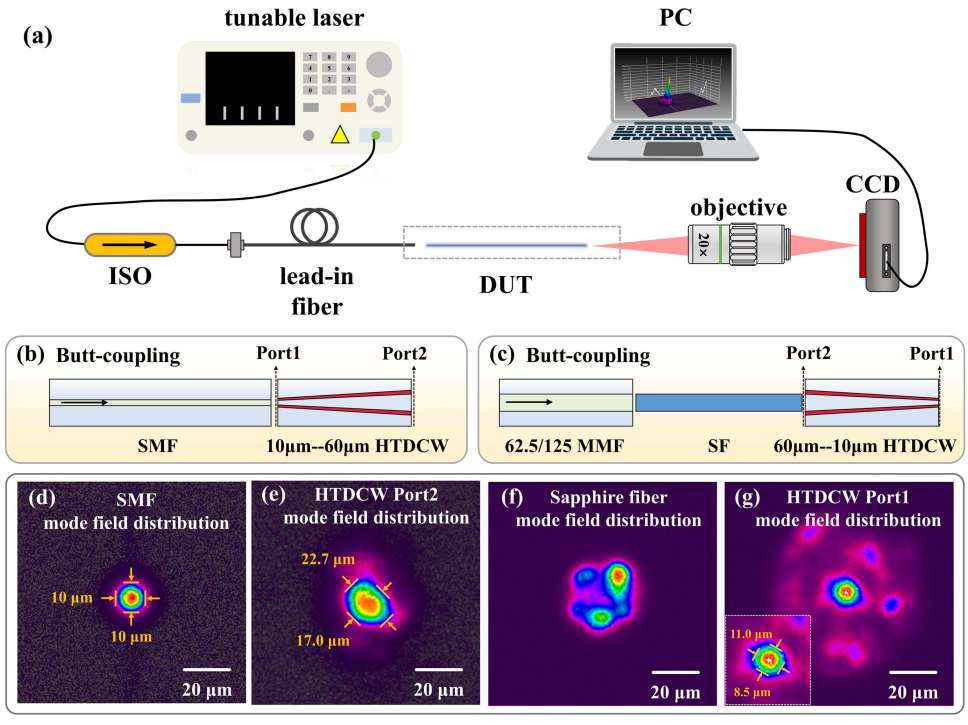

Fig. 4. (a) Experimental setup for the near-field profile of transmission mode measurement. (b), (c) Schematic of butt-coupling measurement method for near-field profiles of SMF, sapphire fiber, and HTDCW. Near-field profiles of transmission mode for (d) SMF, (e) port 2 of HTDCW, (f) sapphire fiber, and (g) port 1 of HTDCW.

SFBG was about 10 cm. The reflection spectra of the SFBG were measured by using a broadband source (Fiber Lake) and an optical spectrum analyzer (OSA, Yokogawa AQ6370C). At first, in the case of T1, the SFBG sample was butt-coupled to 62.5/125 μm MMF, and a 2 × 2, 3 dB 62.5/125 μm MMF coupler was used to connect the broadband source and the OSA. As shown in Fig. 5(a), a Bragg resonance with a broad −3 dB bandwidth [i.e., full-width-at-half-maximum (FWHM)] of 5.08 nm is exhibited, and it results from a large number of modes excited in sapphire fiber and collected by MMF. Then, in the case of T2, an SMF coupler was connected to the measurement system, and the SMF was butt-coupled to the SFBG sample directly. The result illustrates that the −3 dB bandwidth of the reflection spectrum is reduced to 2.09 nm, which indicates that this method can suppress a portion of HOMs. However, some low-order modes with the n_{eff} close to that of the LP_{01} mode remain, resulting in multiple peaks in the reflection spectrum. Finally, in the case of T3, we inserted the HTDCW into the SMF-based measurement system. As a result, we obtained a reflection spectrum with an SNR of 11 dB and a −3 dB bandwidth of 0.62 nm. Hence, as demonstrated by the simulation results in Fig. 2(d) and the near-field profile in Fig. 4(g), the suppression of HOMs reduces the bandwidth, achieving a single-mode spectrum of SFBG. Moreover, compared to the ODC splicing structure [18], this reflection spectrum exhibits more efficient suppression of lower-order modes. Notably, no reflected sidelobes generated by lower-order modes are observed in the spectrum, revealing the higher SNR. Therefore, a reflection spectrum comparable to a single-mode SFBG can be achieved with this method.

Meanwhile, to verify the higher stability of single-mode transmission operation of SFBG in case T3 compared to multimode transmission operation in case T1, we fixed a section of lead-in fiber (i.e., MMF in case T1 and SMF in case T3) to the vibration stage. The vibration frequency and vibration acceleration were set to 20 Hz and 20*g*, corresponding to the vibration frequency of the reactor pressure vessel [39]. The spectrum of SFBG was acquired by OSA, with 65 repeated measurements performed for each test group. The SFBG reflection spectra were subjected to SG filtering and Gaussian fitting for wavelength peak detection. As illustrated in Fig. 5(b), under static conditions, the multimode reflection spectra exhibit more pronounced peak detection instability. The one σ deviation of Bragg wavelength fluctuation in case T1 is ±81.7 pm, which is larger than that of case T3 (i.e., ±5.8 pm). Under the vibration at 20 Hz and 20*g*, the one σ deviation increased in both cases of T1 and T3. However, the single-mode transmission operation of SFBG maintained a one σ deviation of merely ±7.4 pm. It indicated that the single-mode operation SFBG using the proposed method has a better anti-vibration performance for wavelength detection.

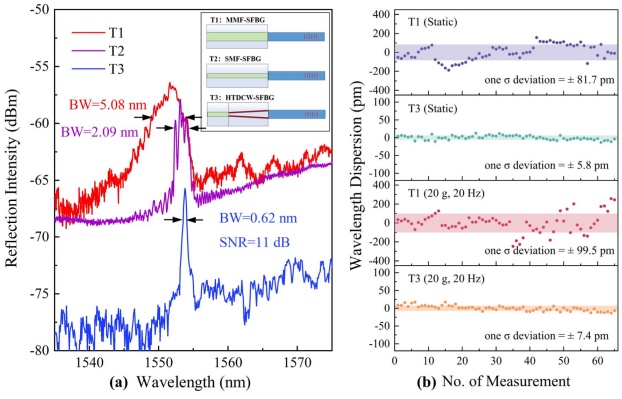

Fig. 5. (a) Reflection spectra of SFBG measured by butt-coupling to MMF, SMF, and HTDCW. Inset: schematic diagram of the SFBG butt-coupled to MMF, SMF, and HTDCW. (b) Wavelength dispersion of 65 measurements for no vibration and at a vibration of 20 Hz.

As shown in Fig. 6(a), the SFBG and the HTDCW were sealed in an argon gas-infiltrated sapphire tube by using a handmade seal device to enhance the durability and stability [10]. As illustrated in the inset of Fig. 6(a), the packaged single-mode SFBG high-temperature sensor consists of an SFBG, an HTDCW, and an SMF jumper. The front-end SFBG and HTDCW were packaged with an argon gas-infiltrated sapphire tube, while the rear-end SMF was packaged with a metal tube (Inconel 600). And the connection was secured by metal fittings and high-temperature ceramic adhesive. Figure 6(b1) displays a micrograph of the sapphire fiber end face polished to 30° using diamond lapping film with a particle size of 3 μm to reduce the surface reflection. Figure 6(b2) shows a micrograph of the line-by-line inscribed SFBG with a grating period of 1.78 μm. Then the sapphire fiber and port 2 of HTDCW were spliced by using a fusion splicer (S178A, Furukawa FITEL) with the splicing parameters set at a discharge intensity of 20 and a discharge time of 80 ms. It can be seen from Figure 6(b3) that the sapphire fiber and the waveguide structure are precisely aligned, and no significant deformation is observed in the HTDCW. Meanwhile, port 1 of HTDCW is also

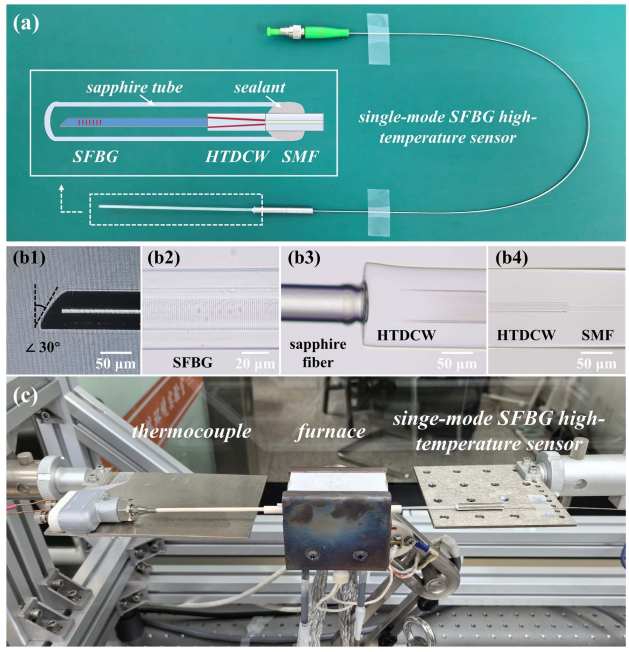

Fig. 6. (a) Photograph of the packaged single-mode SFBG high-temperature sensor. Inset: schematic of the sensor. (b) Microscopy images of the sensor. (c) Photograph of the high-temperature test system.

precisely aligned with the core of SMF to ensure optimal coupling efficiency, as illustrated in Fig. 6(b4). Finally, as shown in Fig. 6(c), temperature response was tested by placing the packaged sensor into a compact high-temperature furnace (THM500, MHI), which is able to reach a maximum temperature of 1600°C. The packaged sensor was connected to the OSA and broadband source with lead-in SMF. A type-B thermocouple was placed in proximity to the sensor to calibrate the temperature. Then, the temperature in the furnace varied from 25°C to 1600°C and was maintained for 30 min at each measurement point.

Figures 7(a) and 7(b) illustrate the smoothed reflection spectra of the SFBG at various temperatures during the heating and cooling processes. It can be observed that the shape and intensity of the reflection spectrum slightly change at various temperatures, but they are relatively stable when the temperature is constant. This might be the reason that the proportion of fundamental mode excited in the sapphire fiber changes, leading to variations in the spectrum. Nevertheless, the characteristic of the reflection peak of the fundamental mode remains quite prominent and the packaged sensor can still stably and clearly detect the peak wavelength at high temperature, which is attributed to the single-mode operation of the SFBG sensor. Then, by recording the changes in the peak wavelength with temperature, we can obtain the temperature response of the sensor, as shown in Fig. 7(c). The peak wavelength of the sensor has a nonlinear thermal response, which can be fit with a polynomial curve. The thermal sensitivities of the SFBG at various temperatures are 23.31 pm/°C at 25°C, 30.18 pm/°C at 800°C, and 35.31 pm/°C at 1600°C. To validate the repeatability of the sensor, two thermal cycling tests were performed. During the two heating and cooling cycles, the Bragg wavelength deviations at different temperature points remained within ±50 pm, corresponding to approximately ±1.6°C. The results demonstrate an excellent consistency between the two cycles. Compared with multimode SFBG, the heating and cooling curves exhibit good repeatability, similar to single-mode SFBG [20,21].

In addition, to characterize the long-term stability of the proposed sensor at high temperature, the long-term stability experiments were conducted at 1500°C for 6 h and 1600°C for 10 h. The spectral data were recorded at 10 min intervals and were subjected to SG filtering and Gaussian fitting for wavelength peak detection. Figures 7(d) and 7(e) display the evolution of peak reflection and Bragg wavelength of the sensor during the long-term high-temperature test. The one σ deviation of the Bragg wavelength under 1500°C and 1600°C is ±14 pm and ±22 pm, respectively. Given a sensitivity coefficient of 35.31 pm/°C at 1600°C, these variations correspond to temperature deviations within ±0.40°C and ±0.62°C, respectively. This performance is significantly better than that of the multimode SFBG sensor [22]. Much of this variation is likely due to the furnace temperature varying during the test. Meanwhile, a slight intensity reduction of approximately 0.5 dB was observed in the reflection peak during long-term testing at both 1500°C and 1600°C, though this will not compromise the demodulation of the sensor. These results exhibit that using the HTDCW and single-mode measurement system has a higher spectral stability compared to that of the multimode fiber measurement system in high-temperature testing. Hence, this approach enables temperature measurements beyond 1200°C, demonstrating enhanced applicability.

4. CONCLUSION

We demonstrated an HTDCW inscribed by femtosecond laser direct writing, which can obtain a single-mode reflection spectrum from SFBG. The diameter of HTDCW was designed and fabricated to increase linearly from 10 μm to 60 μm over a tapered length of 10 mm according to the adiabatic criterion. The near-field profile shows that SMF can realize a better mode field matching with sapphire fiber via HTDCW. And the HTDCW could effectively suppress the HOMs of sapphire fiber. Compared with directly measuring the SFBG reflection spectrum using MMF or SMF, incorporating the HTDCW into the SMF measurement system can provide a narrower bandwidth of 0.62 nm and an enhanced SNR of 11 dB.

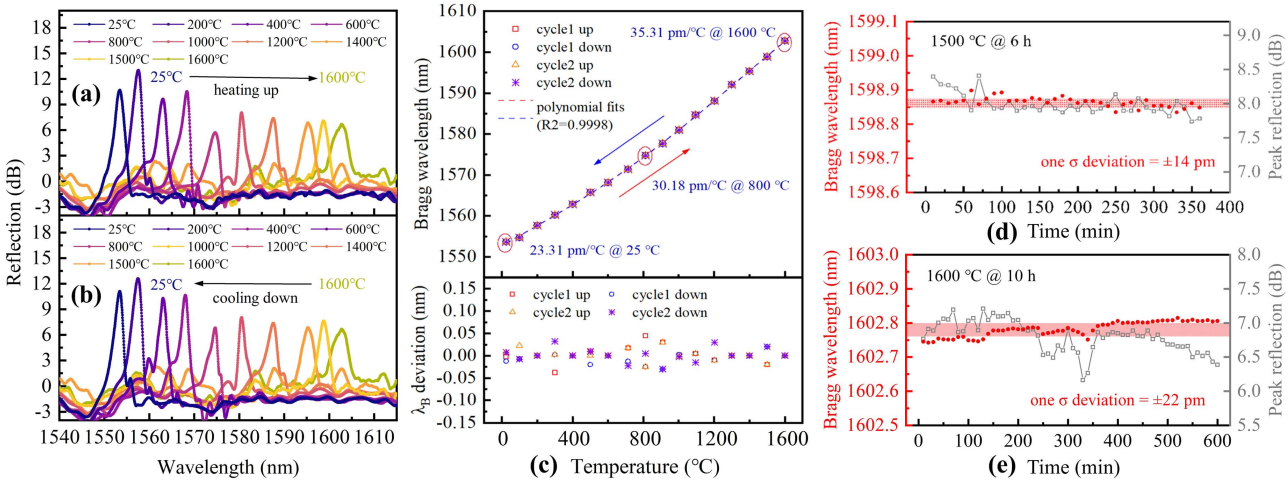

Fig. 7. Evolution of reflection spectra of the sensor during (a) the heating process and (b) the cooling process. (c) Bragg wavelengths of the sensor as a function of temperature for two heating and cooling cycles and Bragg wavelength deviation in two cycles at various temperatures. Change in the Bragg wavelength and peak reflection of the sensor at (d) 1500°C for 6 h and (e) 1600°C for 10 h.

The temperature responses of the SFBG combined with HTDCW using a single-mode demodulation system were investigated. The results exhibit increasing temperature sensitivity at elevated temperatures, i.e., 23.31 pm/°C at 25°C, 30.18 pm/°C at 800°C, and 35.31 pm/°C at 1600°C, and a much better repeatability than the multimode SFBGs. Hence, this single-mode operation SFBG sensor is promising in high-temperature measurement, such as energy, aviation, and gas-fired boilers.

Funding. National Key Research and Development Program of China (2023YFB3208600); National Natural Science Foundation of China (62222510, 62435012, 62375176, T2421003); Guangdong Provincial Department of Science and Technology (2024A1515010108); LingChuang Research Project of China National Nuclear Corporation (CNNC-LCKY-2024-067).

Disclosures. The authors declare no conflicts of interest.

Data Availability. Data underlying the results presented in this paper are not publicly available at this time but may be obtained from the authors upon reasonable request.

REFERENCES

1. Y. Wang, J. E. Ma, and Y. T. Fang, "Generation III pressurized water reactors and China's nuclear power," J. Zhejiang Univ. Sci. A **17**, 911–922 (2016).
2. M. G. Zheng, J. Q. Yan, S. Jun, *et al.*, "The general design and technology innovations of CAP1400," Engineering **2**, 97–102 (2016).
3. S. M. Alshehri, I. A. Said, and S. Usman, "A review and safety aspects of modular high-temperature gas-cooled reactors," Int. J. Energy Res. **45**, 11479–11492 (2021).
4. M. S. Zha, S. P. Zhong, R. C. Chen, *et al.*, "Temperature measuring system of the in-core components for Chinese 10 MW high temperature gas-cooled reactor," J. Nucl. Sci. Technol. **39**, 1086–1093 (2002).
5. A. J. Palmer, R. S. Skifton, D. C. Haggard, *et al.*, "Development and test results of thermocouples used in the TRISO-Fuel irradiation experiment AGR-5/6/7," Nucl. Technol. **209**, 448–470 (2023).
6. P. R. Wang, F. Q. Liu, H. Wang, *et al.*, "A review of third generation SiC fibers and SiC_f/SiC composites," J. Mater. Sci. Technol. **35**, 2743–2750 (2019).
7. S. Gao, X. Q. Zhang, L. W. Chen, *et al.*, "Review: radiation temperature measurement methods for engine turbine blades and environment influence," Infrared Phys. Technol. **123**, 104204 (2022).
8. C. M. Petrie, B. Wilson, and T. E. Blue, "*In situ* gamma radiation-induced attenuation in sapphire optical fibers heated to 1000°C," J. Am. Ceram. Soc. **97**, 3150–3156 (2014).
9. C. M. Petrie and T. E. Blue, "*In situ* reactor radiation-induced attenuation in sapphire optical fibers heated up to 1000°C," Nucl. Instrum. Methods Phys. Res. B **342**, 91–97 (2015).
10. J. He, X. Z. Xu, B. Du, *et al.*, "Stabilized ultra-high-temperature sensors based on inert gas-sealed sapphire fiber Bragg gratings," ACS Appl. Mater. Interfaces **14**, 12359–12366 (2022).
11. J. He, Z. D. Li, X. Z. Xu, *et al.*, "High-temperature strain sensor based on sapphire fiber Bragg grating," Opt. Lett. **49**, 446–449 (2024).
12. T. Habisreuther, T. Elsmann, Z. W. Pan, *et al.*, "Sapphire fiber Bragg gratings for high temperature and dynamic temperature diagnostics," Appl. Therm. Eng. **91**, 860–865 (2015).
13. X. Z. Xu, Q. M. Tan, Z. D. Li, *et al.*, "Sapphire fiber Bragg gratings demodulated with cross correlation algorithm for long-term high-temperature measurement," IEEE Sens. J. **24**, 7905–7911 (2024).
14. M. Busch, W. Ecke, I. Latka, *et al.*, "Inscription and characterization of Bragg gratings in single-crystal sapphire optical fibres for high-temperature sensor applications," Meas. Sci. Technol. **20**, 115301 (2009).
15. Z. D. Li, Q. M. Tan, Z. H. Yan, *et al.*, "Reliable wavelength detection method of sapphire fiber Bragg gratings using added multimode fiber," Opt. Laser Technol. **182**, 112185 (2025).
16. C. Zhan, J. H. Kim, J. Lee, *et al.*, "High temperature sensing using higher-order-mode rejected sapphire-crystal fiber gratings," Proc. SPIE **6698**, 66980F (2007).
17. D. Grobnic, S. J. Mihailov, H. Ding, *et al.*, "Single and low order mode interrogation of a multimode sapphire fibre Bragg grating sensor with tapered fibres," Meas. Sci. Technol. **17**, 980–984 (2006).
18. Q. Bian, H. T. Zhu, J. Q. Liang, *et al.*, "High-order mode suppression in sapphire fiber Bragg gratings based on mode field matching fusion splicing for single-mode demodulation systems," IEEE Sens. J. **23**, 16953–16959 (2023).
19. M. H. Wang, P. S. Salter, F. P. Payne, *et al.*, "Single-mode sapphire fiber Bragg grating," Opt. Express **30**, 15482–15494 (2022).
20. M. H. Wang, P. S. Salter, F. P. Payne, *et al.*, "Single-mode sapphire fiber temperature sensor," J. Lightwave Technol. **42**, 6409–6416 (2024).
21. X. Z. Xu, J. He, J. F. Wu, *et al.*, "Single-mode helical sapphire Bragg grating for high-temperature sensing," J. Lightwave Technol. **43**, 2982–2987 (2025).
22. R. Eisermann, S. Krenek, T. Habisreuther, *et al.*, "Metrological characterization of a high-temperature hybrid sensor using thermal radiation and calibrated sapphire fiber Bragg grating for process monitoring in harsh environments," Sensors **22**, 1034 (2022).
23. C. R. Liao, D. N. Wang, Y. H. Yi, *et al.*, "Temporal thermal response of Type II-IR fiber Bragg gratings," Appl. Opt. **48**, 3001–3007 (2009).
24. M. Lindner, E. Tunc, K. Weraneck, *et al.*, "Regenerated Bragg grating sensor array for temperature measurements during an aluminum casting process," IEEE Sens. J. **18**, 5352–5360 (2018).
25. G. Hawkes, B. Pham, and C. Otani, "Thermal model of the AGR-5/6/7 experiment with offset gas gaps," Nucl. Sci. Eng., 1–26 (2024).
26. C. Feng, D. Li, S. Gao, *et al.*, "Calculating the reflected radiation error between turbine blades and vanes based on double contour integral method," Infrared Phys. Technol. **79**, 171–182 (2016).
27. D. Li, C. Feng, S. Gao, *et al.*, "Effect of pyrometer type and wavelength selection on temperature measurement errors for turbine blades," Infrared Phys. Technol. **94**, 255–262 (2018).
28. J. He, J. He, X. Z. Xu, *et al.*, "Single-mode helical Bragg grating waveguide created in a multimode coreless fiber by femtosecond laser direct writing," Photonics Res. **9**, 2052–2059 (2021).
29. C. Romero, J. G. Ajates, F. Chen, *et al.*, "Fabrication of tapered circular depressed-cladding waveguides in Nd:YAG crystal by femtosecond-laser direct inscription," Micromachines **11**, 10 (2020).
30. S. Sun, X. L. Sun, F. Ren, *et al.*, "Tapered depressed-cladding waveguide lasers modulated by Ag nanoparticles embedded in SiO_2," Results Phys. **30**, 104897 (2021).
31. X. X. Feng, Y. Jiang, S. R. Xie, *et al.*, "Higher-order mode suppression technique for multimode sapphire fiber external Fabry–Perot interferometers," Opt. Express **30**, 4759–4767 (2022).
32. J. D. Love, W. M. Henry, W. J. Stewart, *et al.*, "Tapered single-mode fibres and devices. Part 1: adiabaticity criteria," IEE Proc. Part J. **138**, 343–354 (1991).
33. K. Mishchik, C. D. Amico, P. K. Velpula, *et al.*, "Ultrafast laser induced electronic and structural modifications in bulk fused silica," J. Appl. Phys. **114**, 133502 (2013).
34. B. Zhang, X. F. Liu, and J. R. Qiu, "Single femtosecond laser beam induced nanogratings in transparent media—mechanisms and applications," J. Materiomics **5**, 1–14 (2019).
35. V. R. Bhardwaj, E. Simova, P. B. Corkum, *et al.*, "Femtosecond laser-induced refractive index modification in multicomponent glasses," J. Appl. Phys. **97**, 083102 (2005).

36. D. Z. Tan, X. Y. Sun, J. R. Qiu, *et al.*, "Femtosecond laser writing low-loss waveguides in silica glass: highly symmetrical mode field and mechanism of refractive index change," Opt. Mater. Express **11**, 848–857 (2021).
37. J. F. Wu, X. Z. Xu, C. R. Liao, *et al.*, "Optimized femtosecond laser direct-written fiber Bragg gratings with high reflectivity and low loss," Opt. Express **31**, 3831–3838 (2023).
38. X. Z. Xu, J. He, C. R. Liao, *et al.*, "Multi-layer, offset-coupled sapphire fiber Bragg gratings for high-temperature measurements," Opt. Lett. **44**, 4211–4214 (2019).
39. S. A. Ansari, M. Haroon, A. Rashid, *et al.*, "Measurement and analysis of structural integrity of reactor core support structure in pressurized water reactor (PWR) plant," IEEE Trans. Nucl. Sci. **64**, 844–851 (2017).